

Collapsed upwelling projected to weaken ENSO under sustained warming beyond the twenty-first century

Received: 4 November 2023

Qihua Peng¹, Shang-Ping Xie¹✉ & Clara Deser²

Accepted: 6 June 2024

Published online: 1 July 2024

 Check for updates

The El Niño–Southern Oscillation (ENSO) in a warming climate has been studied extensively, but the response beyond 2100 has received little attention. Here, using long-term model simulations, we find that while ENSO variability exhibits diverse changes in the short term, there is a robust reduction in ENSO variability by 2300. Continued warming beyond 2100 pushes sea surface temperature above the convective threshold over the eastern Pacific, causing collapsed mean equatorial upwelling with intensified deep convection. We show that the weakened thermocline feedback due to the collapsed upwelling and increased thermal expansion coefficient, along with enhanced thermodynamic damping, are crucial to reducing ENSO amplitude under sustained warming. Our results suggest a threshold behaviour in the tropical Pacific, where a convective atmosphere over the eastern equatorial Pacific causes dramatic shifts in ENSO variability. This threshold is not crossed under low-emission scenarios.

The El Niño–Southern Oscillation (ENSO) is the dominant mode of interannual climate variability, characterized by large variations in sea surface temperature (SST) over the tropical Pacific. Potential future changes in ENSO variability due to greenhouse gas increase could have far-reaching impacts on extreme weather, ecosystems and socio-economic conditions around the world^{1,2}. The projected ENSO SST response to global warming remains under debate. While early research based on Coupled Model Intercomparison Project (CMIP) phases 3 and 5 indicates a lack of consensus among climate models regarding the ENSO SST response to global warming^{3–6}, some studies suggest an emerging consensus among models in CMIP6 for increased ENSO SST variability in the twenty-first century^{7–9}. Complicating the matter are recent studies suggesting a reduction in ENSO SST variability under strong CO₂ forcing (for example, 4×CO₂)^{10,11}. These disagreements are probably linked to scenario differences, model generation⁷ and the mean warming patterns⁶.

The projected change in ENSO SST amplitude is time-varying, with an increasing trend before 2040 and a decreasing trend thereafter¹². This underscores the necessity to investigate ENSO responses across various stages of global warming. Most studies have so far

focused on the transient ENSO responses in the twenty-first century or under idealized CO₂ forcings. Nevertheless, how ENSO will respond to sustained high warming beyond the twenty-first century has received little attention. Under high-emission scenarios (RCP8.5 and SSP585), global temperatures are expected to continue rising beyond 2100, with much greater warming magnitudes than in the twenty-first century. This potentially leads to distinct changes in ENSO variability, involving different physical mechanisms. A recent study¹⁰ shows a robust decrease in ENSO amplitude under global warming on millennial horizons, contrasting with the diverse ENSO responses in the twenty-first century. However, limited outputs available within the Long Run Model Intercomparison Project¹³ hinder a rigorous examination of detailed air–sea processes, particularly the role of dynamic adjustments¹⁰. Several explanations—some mutually conflicting—have been proposed to explain the reduced ENSO variability, ranging from a longitudinal variation in the surface warming rate across the Indo-Pacific basin¹² to enhanced thermodynamic damping (TD)¹⁰. Nevertheless, the key ocean–atmospheric processes causing the reduction in ENSO variability under sustained global warming remain unclear.

¹Scripps Institution of Oceanography, University of California San Diego, La Jolla, CA, USA. ²National Center for Atmospheric Research, Boulder, CO, USA.

✉e-mail: sxie@ucsd.edu

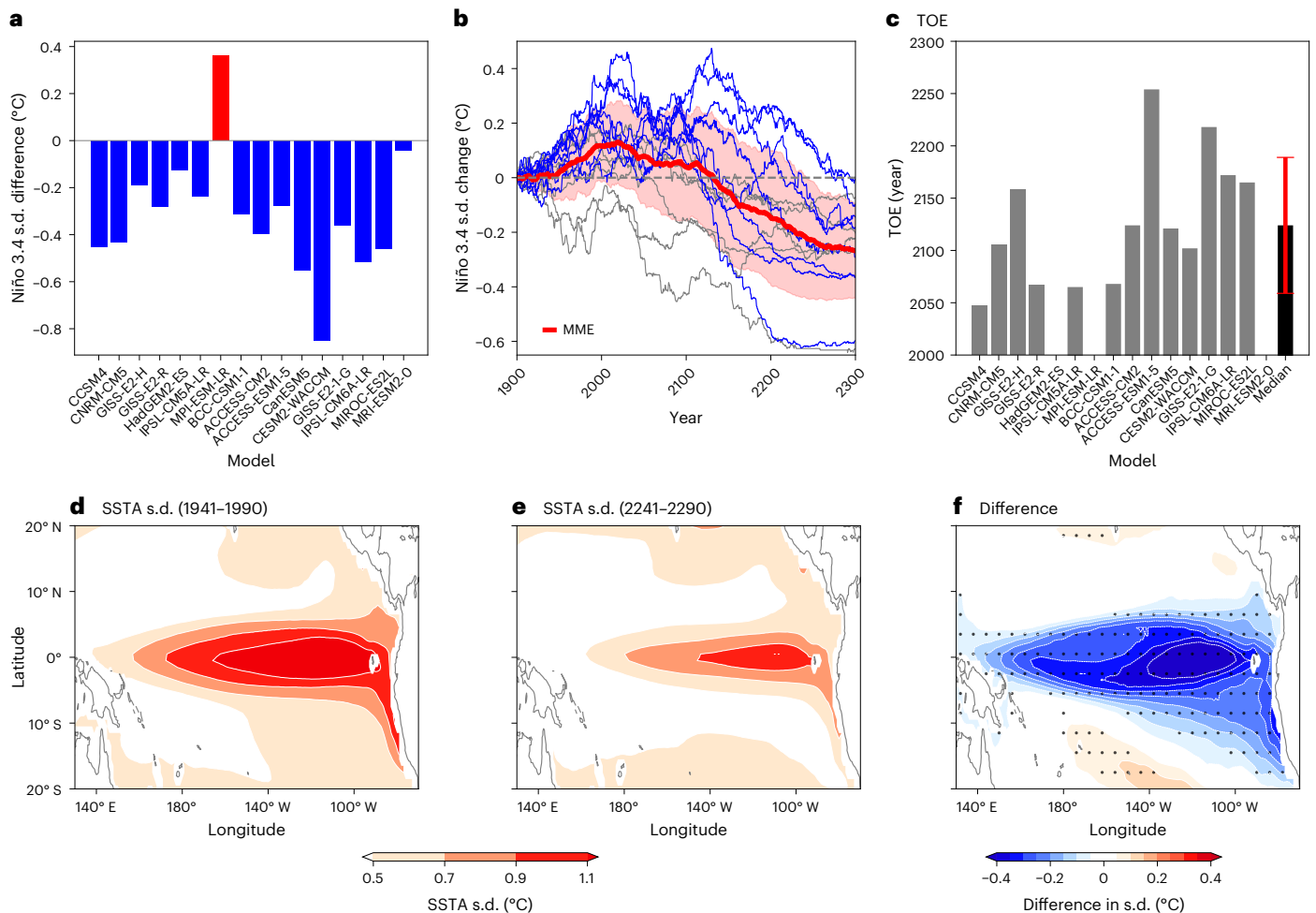


Fig. 1 | ENSO amplitude changes under sustained global warming. **a**, The difference in Niño 3.4 SSTA s.d. (°C) between the twenty-third (2241–2290) and twentieth (1941–1990) centuries under the SSP585/RCP8.5 scenario. **b**, The 50-year running mean ENSO amplitude change (°C) relative to 1850–1900 under SSP585/RCP8.5. The red line represents the MME mean, and the shading indicates one inter-member s.d.; the grey (blue) lines indicate individual models

from CMIP5 (CMIP6). The x axis represents the ending year of each 50-year time window. **c**, TOE of the reduced ENSO variability (grey bars); the black bar indicates the median value, and the error bar represents the interquartile range ($n = 15$). **d–f**, The SST s.d. for the present day (1941–1990) (**d**), the future period (2241–2290) (**e**) and their difference (**f**). The stippling indicates a significant difference at the 95% confidence level from the bootstrap test.

The present study aims to gain insights for a more comprehensive understanding of the coupled dynamics of ENSO change under sustained global warming. On the basis of climate model simulations extended to 2300, we find a consistent reduction in ENSO variability under high CO₂ emissions during 2241–2290 when compared with the present-day climate. Our results highlight that collapsed upwelling and an increased thermal expansion coefficient will weaken the thermocline feedback, which, in conjunction with enhanced TD, are crucial to reducing ENSO SST variability under sustained warming. Importantly, we reveal that these dynamic and thermodynamic adjustments are closely linked to the transition of the equatorial cold tongue into a warm and convective mean state.

Suppressed ENSO variability

We analysed 16 available climate models with extension runs to 2299 or 2300 under high-emission scenarios (RCP8.5 and SSP585) from CMIP5 and CMIP6. In these extension runs, anthropogenic radiative forcing continues to increase beyond 2100, reaching slightly above 12 W m⁻² in 2250 and subsequently levelling off⁴⁴ (see the details in Methods). The climate models reasonably simulate the present-day ENSO with large SST variance in the central and eastern Pacific Ocean as in observations (Fig. 1d). We investigated the ENSO response to

substantial global warming by contrasting its monthly SST anomaly (SSTA) standard deviation (s.d.) in the present day (1941–1990) with that in the twenty-third century (2241–2290) in each climate model.

Fifteen out of 16 models see a robust decrease in Niño 3.4 SST variability during 2241–2290 (Fig. 1a), statistically significant above the 95% confidence level from a bootstrap test (Extended Data Fig. 1a). The only exception is MPI-ESM-LR. As an earlier CMIP5 model, MPI-ESM-LR shows limited skill in simulating present-day El Niño, with two warming centres in the eastern and western Pacific, contrasting with other models (Extended Data Fig. 2). Hereafter, we excluded this model from further analysis. For the remaining 15 models, the multi-model ensemble (MME) mean decrease in Niño 3.4 amplitude is 41% ± 18%. Specifically, the ENSO amplitude initially undergoes a slight increase up to ~2020 (Fig. 1b) and then gradually decreases towards the current level in the early 2100s, with considerable inter-model differences (Extended Data Fig. 1b)^{12,15}. Around 2120, the ENSO amplitude undergoes a rapid decrease, and by 2300, there is a consistent decrease in ENSO amplitude with high inter-model consensus (Fig. 1a,b). The SST variance pattern over the tropical Pacific Ocean does not change much, which can be represented by the Niño 3.4 index (Fig. 1e,f). Note that our assessment of ENSO variability change employs monthly SSTA s.d., with potential impacts from ENSO seasonality change. The reduced ENSO amplitude

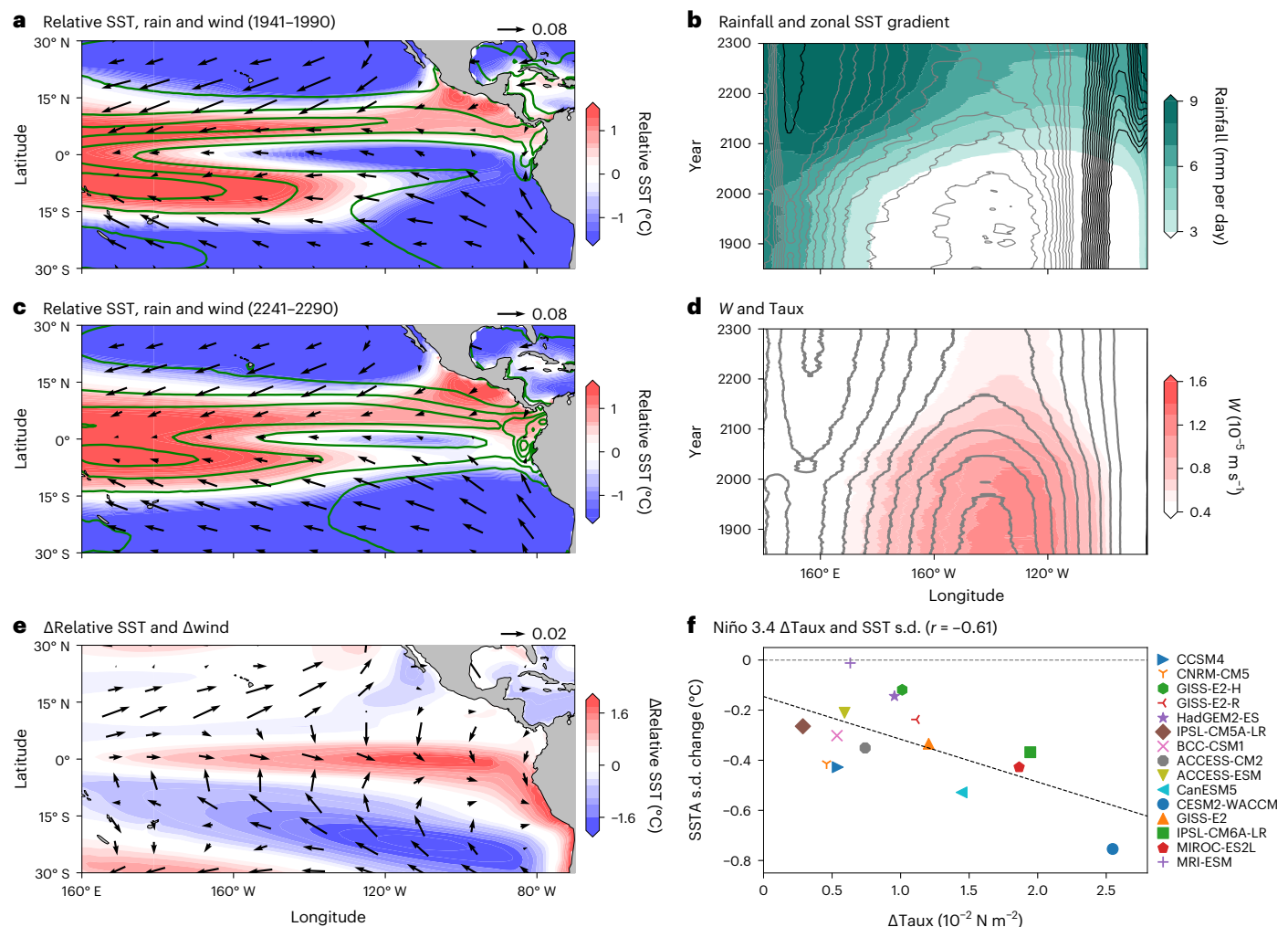


Fig. 2 | Mean state changes in the tropical Pacific. **a, c, e**, Annual mean SST ($^{\circ}\text{C}$, coloured shading), rainfall (contours with an interval of 3 mm per day) and wind stress (N m^{-2} , vectors) for the present day (1941–1990) (**a**), the future (2241–2290) (**c**) and their difference (future minus present day) (**e**). **b, d**, Longitude–time evolution at the Equator of rainfall (mm per day, coloured shading) and zonal SST gradient for each grid point (here we computed $d\text{SST}/dx$ at each grid box along the Equator; contours with an interval of 0.005°C per degree, positive in black

and negative in grey; negative values indicate cooler temperatures in the east) (**b**), and mean equatorial upwelling at 60 m derived only from the models with direct vertical velocity outputs (W ; 10^{-5} m s^{-1} , coloured shading; Methods and Supplementary Table 1) and zonal wind stress (Taux; contours with an interval of 0.01 N m^{-2} ; positive in black and negative in grey) (**d**), all meridionally averaged in 2°S – 2°N . **f**, Scatter plots of Niño 3.4 averaged Δ Taux (10^{-2} N m^{-2} , vectors) and SSTA s.d. changes from SSP585/RCP8.5 extended simulations.

is evident across almost all the models when ENSO seasonality change is considered (Extended Data Fig. 3). The decreased ENSO variability on multi-century horizons is also evident in ACCESS-ESM1-5 large ensemble experiments: all the ensemble members project reduced ENSO variations during 2241–2290, with an ensemble mean decrease of -16% (Extended Data Fig. 4a).

We investigated the time of emergence (TOE) of the reduction in ENSO variability (Methods). Our results reveal that weakened ENSO variability would start to emerge above the background noise around the 2120s, with a median TOE of 2124 (interquartile range, 2059–2189). However, the TOE exhibits sizeable inter-model differences. Eight models project reduced ENSO variability in the twenty-first century, and five of them show weakened ENSO variability emerging above the background noise before 2100. This inter-model difference may be closely linked to model generation. Specifically, the TOE from CMIP5 models (median, 2068) generally precedes that from CMIP6 models (median, 2168) (Fig. 1b,c). This much earlier (later) TOE in CMIP5 (CMIP6) would lead to more (fewer) models exhibiting reduced ENSO variabilities in the twenty-first century. This systematic TOE difference seems to be related to the recent finding that more models project

increased ENSO variability in the twenty-first century in CMIP6 than in the CMIP5 ensemble^{7–9}. More research is needed to elucidate the underlying physical processes.

Mean state changes

The response of ENSO variability to global warming is closely linked to changes in the mean state^{4,16,17}. In the current climate, the prevailing easterly winds in the equatorial Pacific Ocean shoal the thermocline and upwell cold water, forming the familiar equatorial ‘cold tongue’ in SST. Consequently, deep convection in the eastern tropical Pacific is strongly suppressed, accompanied by strong trade winds (Fig. 2a) and intense upwelling.

All the 16 climate models project an El Niño-like warming pattern during 2241–2290 (Fig. 2e and Extended Data Fig. 1c), similar to that in the twenty-first century^{18,19} but with much larger amplitudes. Atmospheric convective instability in the eastern Pacific is measured by the local SST deviation from the tropical mean over 20°S – 20°N (ref. 6), which is taken as the convective threshold²⁰. The MME relative SST in the eastern Pacific remains negative through the twenty-first century (Fig. 3a), indicating suppressed deep convection. However,

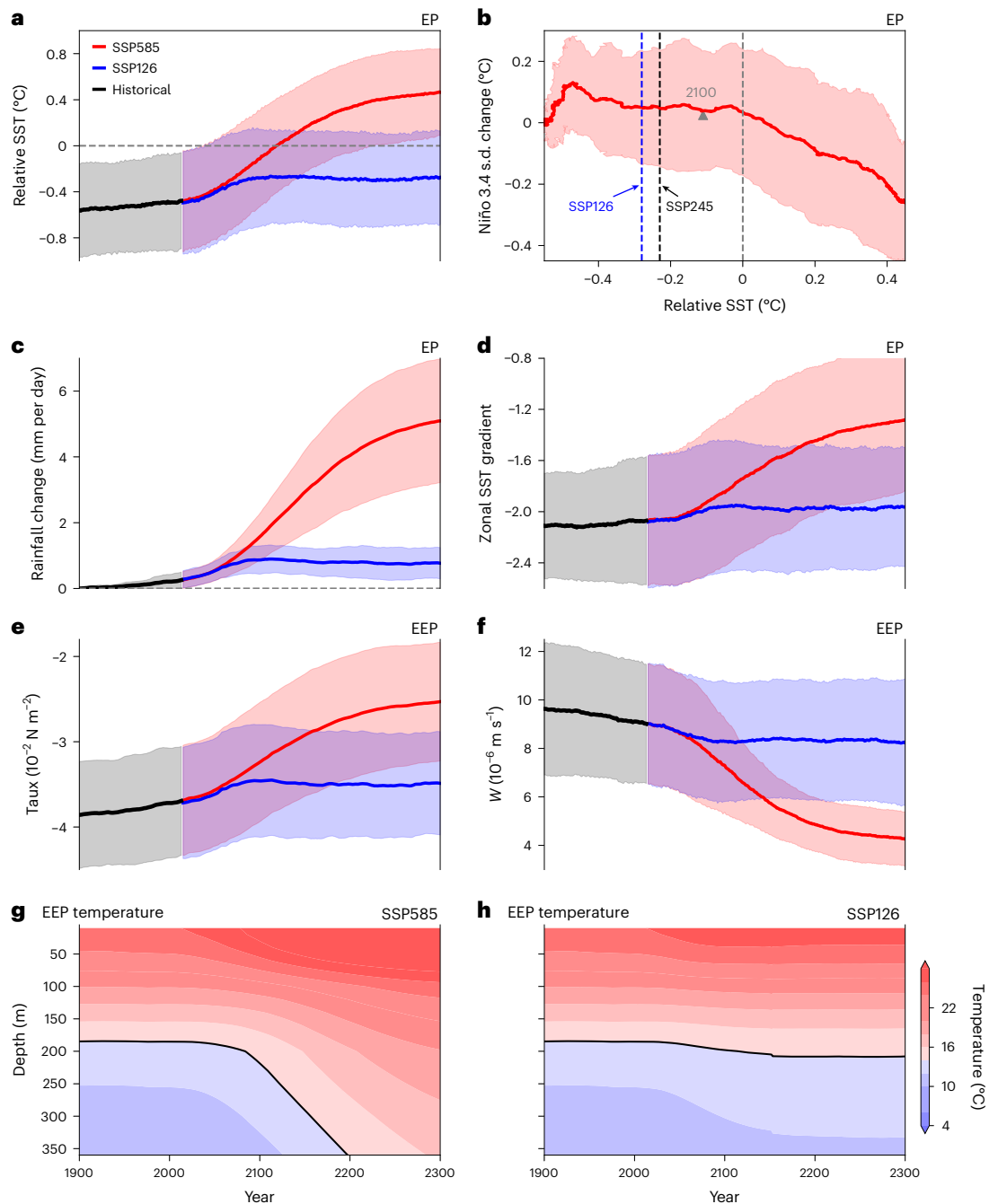


Fig. 3 | Eastern equatorial Pacific mean state changes. **a**, The 50-year running mean relative SST ($^{\circ}\text{C}$; defined as the deviation from the tropical mean over 20°S – 20°N) averaged over the eastern Pacific (EP) region (170°W – 90°W , 5°S – 5°N) from the historical (black), SSP585/RCP8.5 (red) and SSP126/RCP2.6 (blue) simulations. **b**, Relationship between EP relative SST ($^{\circ}\text{C}$) and the Niño 3.4 s.d. change during 1850–2300 from historical and SSP585/RCP8.5 runs; the triangle represents the relative SST in 2100. The dashed blue (black) line indicates the EP relative SST in the twenty-third century under the SSP126/RCP2.6 (SSP245/RCP4.5) scenario. **c**, **d**, Same as **a** but for EP rainfall changes and zonal SST gradient, respectively. Here zonal SST gradient change is defined as

the SST change difference ($^{\circ}\text{C}$) between the eastern (120°W – 170°W , 5°S – 5°N) and western (150°E – 170°W , 5°S – 5°N) boxes, with positive values indicating an El Niño-like warming pattern. **e**–**h**, The evolution of Taux (10^{-2}N m^{-2}) (**e**), mean upwelling (10^{-6}m s^{-1} , derived from models with direct vertical velocity outputs; Methods) (**f**) and ocean temperature (coloured shading) with the 14°C isotherm (black line) under SSP585/RCP8.5 (**g**) and SSP126/RCP2.6 (**h**) in the eastern equatorial Pacific (EEP; 170°W – 90°W , 2°S – 2°N). The coloured shading indicates the spread of one s.d. among inter-members. The x axis indicates the ending year of each 50-year time window.

the El Niño-like warming pattern causes the relative SST to increase and ultimately turn positive around the mid-twenty-second century. In the eastern Pacific, when SST exceeds the convective threshold, deep convection develops (Figs. 2b and 3c). This causes gradual intrusion of rainfall and westerly wind anomalies into the eastern Pacific (Fig. 2b,d). The westerly wind changes effectively reduce the equatorial

upwelling (Fig. 2d) and further warm up the upper ocean in the eastern Pacific (Fig. 3g), forming a positive feedback. Consequently, there is a notable reduction in the trade winds and mean equatorial upwelling during 2241–2290 (Fig. 3f). The strongly relaxed trade winds cause the background upwelling to weaken by a factor of four in the central equatorial Pacific (Fig. 2d), a change large enough to be called a

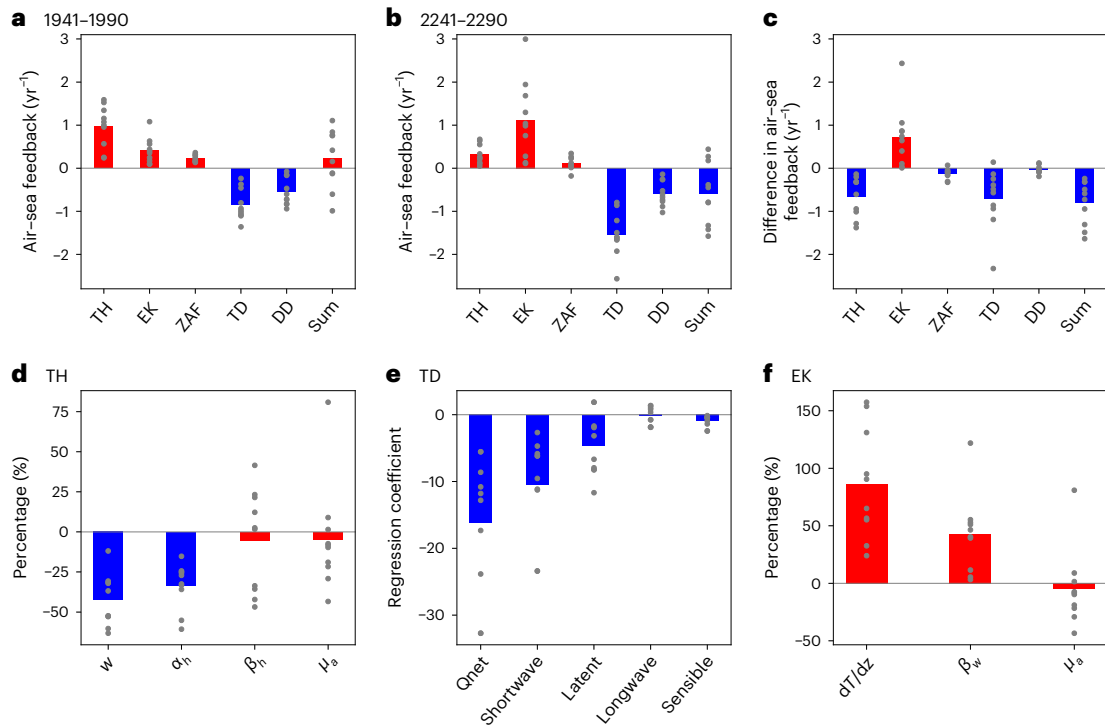


Fig. 4 | ENSO-related air-sea feedback changes. **a–c**, The MME ($n = 10$) ENSO-related air-sea feedbacks (yr^{-1}) (bars; see Methods) in the eastern Pacific ($5^\circ \text{S}–5^\circ \text{N}$, $90^\circ \text{W}–170^\circ \text{W}$) for the present day (1941–1990) (**a**), the future (2241–2290) (**b**) and their difference (**c**). TH, EK, ZAF, TD and DD represent the thermocline feedback, Ekman feedback, zonal advective feedback, thermodynamic damping and dynamic damping, respectively. **d**, The contribution of mean upwelling (W), the subsurface temperature response to SLA (Kelvin waves) (α_h) in the eastern Pacific Ocean, the zonal SLA slope response

to anomalous equatorial wind forcing (β_w) and the equatorial wind response to eastern SSTA forcing (μ_w) in reducing the thermocline feedback. **e**, The relative importance of each heat flux component in modulating the TD feedback, which is represented by the regression coefficient of the heat flux (W m^{-2}) with respect to Niño 3.4 SST ($^\circ \text{C}$) anomalies. **f**, The contributions of vertical stratification (dT/dz), upwelling response to anomalous equatorial wind forcing (β_w), and μ_w in enhancing the EK feedback. The dots indicate the results from the ten individual models with positive Niño 3 skewness (Methods).

collapse. Notably, even under sustained warming, the trade winds and upwelling do not vanish entirely (Fig. 3f) due to the meridional advection of easterly momentum to the Equator during much of the year by the climatological cross-equatorial winds (Extended Data Fig. 1d)²¹. These mean state changes lead to drastic shifts in the eastern tropical Pacific from a dynamic perspective: the cold tongue with its suppressed convection transitions to a basin-wide warm and convective state with distinct air-sea interactions. The strong ocean warming and collapsed upwelling at the Equator weaken ENSO variability as shown below.

Physical mechanisms

To investigate physical processes underlying the robust reduction in ENSO variability, we quantified the relative importance of each dynamic and thermodynamic feedback for the change between the present day (1941–1990) and the future (2241–2290). Here we mainly focused on ten models that produce positive Niño 3 skewness as observed (Methods and Supplementary Table 1). The thermocline feedback dominates the present-day ENSO (Fig. 4a), consistent with observations^{22,23}. The reduced ENSO variability during 2241–2290 is primarily due to the reduced thermocline feedback and enhanced TD (Fig. 4c) with high inter-model consistency (Extended Data Fig. 5).

Thermocline feedback refers to the effect of thermocline displacements on SST variability in the presence of background upwelling. Various definitions of the thermocline can lead to different, sometimes mutually contradicting, conclusions regarding changes in thermocline depth^{10,24,25} and ENSO feedbacks in a warming climate. We sidestepped this issue and used sea level anomaly (SLA) instead to evaluate the thermocline feedback across different time periods in model projections. The SLA is equivalent to vertically integrated subsurface temperature

disturbances due mostly to thermocline displacements, and its zonal gradient is nearly in balance with the zonal wind on the interannual timescales. The weakened thermocline feedback is dominated by the mean upwelling term (W) and the subsurface temperature response term (α_h) (Fig. 4d). Regarding the former, the strong El Niño-like warming pattern during 2241–2290 leads to substantially weakened equatorial upwelling, which limits the vertical advection of subsurface temperature anomalies into the surface layer and thus reduces the SST response to thermocline displacements. Indeed, models with a larger reduction in the mean trade winds feature a stronger reduction in ENSO variability (Fig. 2f), with an inter-model correlation of -0.61 , statistically significant above the 95% confidence level. This supports the idea that the reduced ENSO variability during 2241–2290 is closely linked to the weakened mean equatorial upwelling.

Equally important for the thermocline feedback change is the robust decrease in the eastern Pacific subsurface temperature sensitivity to a given SLA (or α_h) in a warming climate (Figs. 4c and 5) as the thermal expansion coefficient (α) of water increases with temperature²⁶, from 2.1×10^{-4} at present to $2.7 \times 10^{-4} \text{ } ^\circ \text{C}^{-1}$ in 2300 (Extended Data Fig. 6b). Models with a larger α increase tend to generate a greater reduction in ENSO variability, and vice versa, and this relationship is statistically significant above the 95% confidence level (Extended Data Fig. 6a). Specifically, the zonal momentum balance dictates that the SLA tilt response to wind stress anomalies (β_w) changes little (Fig. 4d), but with a larger thermal expansion coefficient in a warming ocean, the same SLA (or steric height) corresponds to a smaller subsurface temperature anomaly (Extended Data Fig. 6d), leading to a reduction in α_h in the twenty-third century (Fig. 4d). Indeed, subsurface temperature responses to a given SLA of an El Niño during 2241–2290 are notably

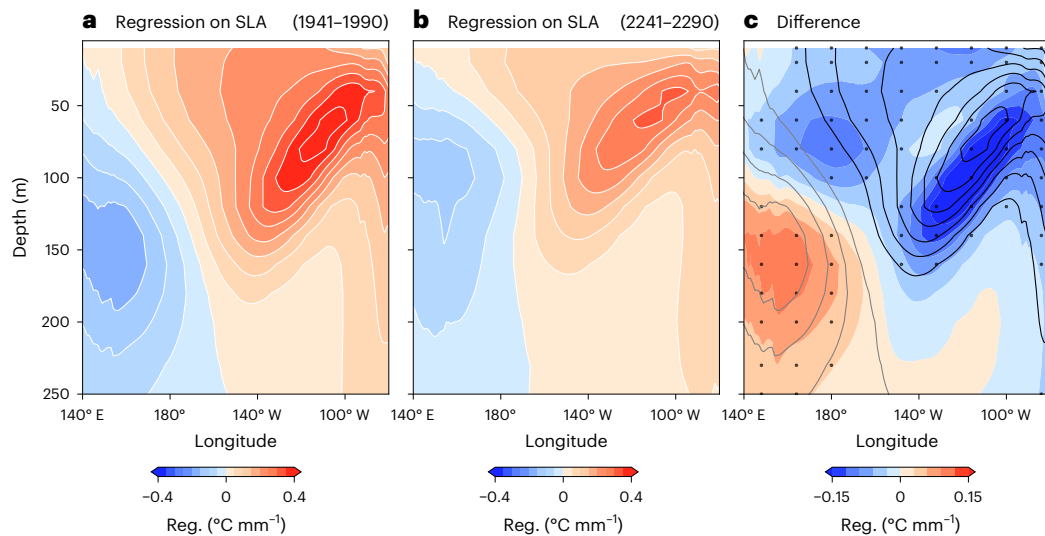


Fig. 5 | Changes in subsurface temperature anomalies due to the increased thermal expansion coefficient. **a–c**, Regression of ocean temperature ($^{\circ}\text{C}$) anomalies onto EP (90°W – 170°W , 5°S – 5°N) SLA variability (mm) for the present day (1941–1990) (**a**), the future (2241–2290) (**b**) and their difference (**c**). The contour lines in **c** denote the present-day regression coefficient (at $0.1^{\circ}\text{C mm}^{-1}$

intervals; positive in black and negative in grey). All these results are derived from the ten models exhibiting positive Niño 3 skewness (Methods). The stippling denotes differences that are significant at the 95% confidence level from the bootstrap test.

smaller than at present (Fig. 5 and Extended Data Fig. 6c). Together, the collapsed mean upwelling and the increased thermal expansion coefficient weaken the thermocline feedback in a warmer climate, leading to a substantial decrease in ENSO SST variability.

The enhanced TD is another important mechanism for inhibiting ENSO variability (Fig. 4c)¹⁰. SST variability in the eastern Pacific is associated with more heat loss to the atmosphere during 2241–2290 than during 1941–1990, primarily due to stronger damping effects of shortwave radiation and latent heat flux (Fig. 4e and Extended Data Fig. 7). These heat flux changes are due to the background El Niño-like warming pattern under sustained global warming: the faster central-eastern Pacific warming pushes the background SST above the convective threshold. Consequently, relatively small central and eastern Pacific SST anomalies during 2241–2290 lead to large deep convection and rainfall anomalies^{6,27}. For El Niño events during 2241–2290, the increased convective response to central and eastern Pacific SST warming strongly reduces downward shortwave radiation and cools SST there (Extended Data Fig. 7c,d). Moreover, saturation vapour pressure increases with temperature (the Clausius–Clapeyron equation), and so does the evaporative damping for ENSO (Extended Data Fig. 7b).

In the present-day climate, the thermocline feedback in models with negative Niño 3 skewness is only ~30% of that in models with positive skewness (Extended Data Fig. 8d) and observations¹². Consequently, the change in thermocline feedback is also smaller in these models with negative skewness, where the reduced ENSO amplitude primarily results from the enhanced TD (Extended Data Fig. 8f). This highlights the need for realistic simulation of nonlinear ENSO processes.

Threshold behaviour for rapid reduction in ENSO variability

Both the weakened thermocline feedback and enhanced TD are intricately connected to the transition of the eastern Pacific from a cold, non-convective state to a warm, convective state. Consequently, in relative SST space, ENSO variance drops precipitously when the eastern Pacific enters a convective state (Fig. 3b). ENSO dynamics also undergo drastic changes, from a thermocline-feedback-dominant regime at present to an Ekman-feedback-dominant regime during 2241–2290 (Fig. 4a,b). We therefore suggest that the convective threshold,

as represented by relative SST and precipitation in the cold tongue region, is a potential key point at which ENSO and equatorial Pacific climate undergo dramatic shifts. The following comparison with more moderate warming scenarios corroborates such convective threshold behaviour.

The first example is diverse projected changes in the twenty-first century: CMIP3 and CMIP5 models disagree on the sign of projected ENSO change^{3–6}, but recent studies suggest an inter-model consensus on increased ENSO SST variability among CMIP6 models^{7–9}. Beyond the twenty-first century, both the CMIP5 and CMIP6 ensembles consistently project a substantial reduction in ENSO SST amplitude under SSP585/RCP8.5. While anthropogenic warming in the twenty-first century results in weakening of mean equatorial upwelling and warming of the eastern Pacific upper ocean, the magnitudes of these changes are relatively small (Fig. 3f,g). The resulting ENSO variability reduction might counteract other ENSO-amplifying effects such as increased air–sea coupling⁷, or it could be too subtle to distinguish from the sizeable ensemble spread originating from inter-model differences or internal variability. This leads to diverse ENSO responses among different models in the twenty-first century in a combined CMIP5–CMIP6 ensemble (Extended Data Fig. 1b). However, beyond the twenty-first century, the eastern Pacific mean SST continues to rise and exceeds the convective threshold (Fig. 3a). The resultant reduced thermocline feedback and enhanced TD dominate over other processes, ultimately leading to a robust decrease in ENSO amplitude in the twenty-third century.

Another example is the distinct ENSO responses under moderate warming scenarios. We compared extension runs under SSP126/RCP2.6 and SSP245/RCP4.5 (see the details in Methods). There is a lack of inter-model consensus on changes in ENSO SST variability by 2300 under either the SSP126/RCP2.6 (Extended Data Figs. 4b and 9a) or SSP245/RCP4.5 (Extended Data Fig. 10a) scenario. These results indicate that the ENSO variance change beyond the twenty-first century is scenario-dependent: the robust reduction in ENSO amplitude is apparent only in high- CO_2 -emission scenarios. The MME-mean relative SST in the eastern Pacific under low-emission scenarios remains negative through the twenty-third century (Fig. 3a and Extended Data Fig. 10c), indicating continued suppression of convective activity in the eastern Pacific. This implies that the limited warming under SSP126/RCP2.6 or SSP245/RCP4.5 is generally insufficient to trigger

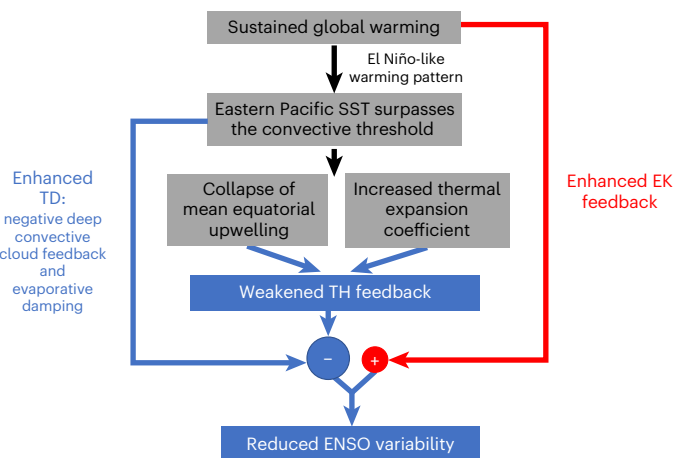


Fig. 6 | Reduced ENSO variability under sustained global warming. Blue (red) represents the physical processes that inhibit (amplify) ENSO variability. The size of the circles indicates the strength of their influence on ENSO variability. Sustained greenhouse warming induces El Niño-like warming and pushes eastern Pacific SST beyond the convective threshold. On the one hand, this induces the collapse of equatorial mean upwelling and strong upper ocean warming with an increased thermal expansion coefficient. These mean state changes largely reduce the thermocline feedback during 2241–2290. On the other hand, the convective eastern Pacific mean state strongly enhances TD. During 2241–2300, relatively small SST warming perturbations of ENSO could induce large rainfall responses, which reduces downward shortwave radiation (deep convective cloud feedback) and cools SST there. Evaporative damping also enhances due to strong background SST warming. Taken together, the reduced thermocline feedback and enhanced TD work together and efficiently reduce ENSO variability. Despite the enhanced EK feedback due to increased vertical stratification amplifying ENSO variation, its contribution is relatively small. We consequently find a net decrease in ENSO variability under sustained warming.

the convective threshold behaviour, preventing a dramatic shift in the eastern Pacific mean state. The deep convection in the eastern Pacific is still suppressed during 2241–2290 (Extended Data Figs. 9b and 10b), together with persistent easterly trade winds (Fig. 3e and Extended Data Fig. 10d). These moderate mean-state perturbations lead to small changes in equatorial mean upwelling (Fig. 3f) and upper ocean temperature (Fig. 3h), with relatively small impacts on the ocean–atmosphere coupling processes (Extended Data Fig. 9d). Consequently, the resultant ENSO changes fail to surpass other factors, such as inter-model differences or internal variability. This leads to divergent projections of ENSO amplitude changes under low-emission scenarios.

Discussion

Diverse changes in ENSO amplitude were projected among CMIP3 and CMIP5 models^{3–6}, although a tendency for increased ENSO variability in the twenty-first century emerged in CMIP6 models^{7–9}. We show a robust decrease in ENSO SST variation under sustained substantial global warming in the twenty-third century^{10,12}. The ocean–atmospheric processes that contribute to this ENSO variance reduction are summarized in Fig. 6. As the eastern Pacific Ocean surpasses the convective threshold under sustained global warming, it transitions from low SSTs with suppressed convection in the present climate to a basin-wide warm and convective state, accompanied by collapsed equatorial upwelling. This change, together with the increased thermal expansion coefficient, efficiently weakens the thermocline feedback. Furthermore, a convective eastern Pacific strongly enhances TD: relatively small SST anomalies in the eastern Pacific during El Niño events in the twenty-third century lead to large convective rainfall anomalies, causing a strong reduction in downward shortwave radiation and cooling SST. Thus, both the dynamic and thermodynamic adjustments,

which are closely linked to mean state shifts to a convective eastern Pacific, act to reduce ENSO amplitude under sustained warming. These results highlight dramatic shifts in ENSO variability and equatorial Pacific climate upon exceeding the convective threshold. Only substantial warming under high-emission scenarios beyond the twenty-first century can raise eastern Pacific SST above the convective threshold. This explains why the projected decrease in ENSO variability does not emerge in the twenty-first century or under low-emission scenarios (for example, SSP126 or SSP245). These results could provide insights for a more comprehensive understanding of ENSO dynamics and more reliable projections of ENSO change in a warming climate.

Online content

Any methods, additional references, Nature Portfolio reporting summaries, source data, extended data, supplementary information, acknowledgements, peer review information; details of author contributions and competing interests; and statements of data and code availability are available at <https://doi.org/10.1038/s41558-024-02061-8>.

References

- McPhaden, M. J., Zebiak, S. E. & Glantz, M. H. ENSO as an integrating concept in Earth science. *Science* **314**, 1740–1745 (2006).
- Philander, S. G. El Niño, La Niña, and the southern oscillation. *Int. Geophys. Ser.* **46**, X-289 (1989).
- Collins, M. et al. The impact of global warming on the tropical Pacific ocean and El Niño. *Nat. Geosci.* **3**, 391–397 (2010).
- Latif, M. & Keenlyside, N. S. El Niño/Southern Oscillation response to global warming. *Proc. Natl Acad. Sci. USA* **106**, 20578–20583 (2009).
- Stevenson, S. Significant changes to ENSO strength and impacts in the twenty-first century: results from CMIP5. *Geophys. Res. Lett.* **39**, L17703 (2012).
- Zheng, X.-T., Xie, S.-P., Lv, L.-H. & Zhou, Z.-Q. Intermodel uncertainty in ENSO amplitude change tied to Pacific Ocean warming pattern. *J. Clim.* **29**, 7265–7279 (2016).
- Cai, W. et al. Increased ENSO sea surface temperature variability under four IPCC emission scenarios. *Nat. Clim. Change* **12**, 228–231 (2022).
- Fredriksen, H. B., Berner, J., Subramanian, A. C. & Capotondi, A. How does El Niño–Southern Oscillation change under global warming—a first look at CMIP6. *Geophys. Res. Lett.* **47**, e2020GL090640 (2020).
- Yun, K.-S. et al. Increasing ENSO–rainfall variability due to changes in future tropical temperature–rainfall relationship. *Commun. Earth Environ.* **2**, 43 (2021).
- Callahan, C. W. et al. Robust decrease in El Niño/Southern Oscillation amplitude under long-term warming. *Nat. Clim. Change* **11**, 752–757 (2021).
- Wengel, C. et al. Future high-resolution El Niño/Southern Oscillation dynamics. *Nat. Clim. Change* **11**, 758–765 (2021).
- Kim, S. T. et al. Response of El Niño sea surface temperature variability to greenhouse warming. *Nat. Clim. Change* **4**, 786–790 (2014).
- Rugenstein, M. et al. LongRunMIP: motivation and design for a large collection of millennial-length AOGCM simulations. *Bull. Am. Meteorol. Soc.* **100**, 2551–2570 (2019).
- van Vuuren, D. P. et al. The representative concentration pathways: an overview. *Climatic Change* **109**, 5–31 (2011).
- Maher, N. et al. The future of the El Niño–Southern Oscillation: using large ensembles to illuminate time-varying responses and inter-model differences. *Earth Syst. Dyn.* **14**, 413–431 (2023).
- Collins, M. The El Niño–Southern Oscillation in the second Hadley Centre coupled model and its response to greenhouse warming. *J. Clim.* **13**, 1299–1312 (2000).

17. Timmermann, A. et al. Increased El Niño frequency in a climate model forced by future greenhouse warming. *Nature* **398**, 694–697 (1999).
 18. Heede, U. K. & Fedorov, A. V. Towards understanding the robust strengthening of ENSO and more frequent extreme El Niño events in CMIP6 global warming simulations. *Clim. Dyn.* **61**, 3047–3060 (2023).
 19. Xie, S. P. et al. Global warming pattern formation: sea surface temperature and rainfall. *J. Clim.* **23**, 966–986 (2010).
 20. Johnson, N. C. & Xie, S.-P. Changes in the sea surface temperature threshold for tropical convection. *Nat. Geosci.* **3**, 842–845 (2010).
 21. Okumura, Y. & Xie, S.-P. Interaction of the Atlantic equatorial cold tongue and the African monsoon. *J. Clim.* **17**, 3589–3602 (2004).
 22. Lubbecke, J. F. & McPhaden, M. J. Assessing the twenty-first-century shift in ENSO variability in terms of the Bjerknes Stability Index*. *J. Clim.* **27**, 2577–2587 (2014).
 23. Peng, Q. et al. Eastern Pacific wind effect on the evolution of El Niño: implications for ENSO diversity. *J. Clim.* **33**, 3197–3212 (2020).
 24. Crespo, L. R. et al. Weakening of the Atlantic Niño variability under global warming. *Nat. Clim. Change* **12**, 822–827 (2022).
 25. Yang, Y. et al. Suppressed Atlantic Niño/Niña variability under greenhouse warming. *Nat. Clim. Change* **12**, 814–821 (2022).
 26. Widlansky, M. J., Long, X. & Schloesser, F. Increase in sea level variability with ocean warming associated with the nonlinear thermal expansion of seawater. *Commun. Earth Environ.* **1**, 9 (2020).
 27. Cai, W. et al. Increasing frequency of extreme El Niño events due to greenhouse warming. *Nat. Clim. Change* **4**, 111–116 (2014).
- Publisher's note** Springer Nature remains neutral with regard to jurisdictional claims in published maps and institutional affiliations.
- Springer Nature or its licensor (e.g. a society or other partner) holds exclusive rights to this article under a publishing agreement with the author(s) or other rightsholder(s); author self-archiving of the accepted manuscript version of this article is solely governed by the terms of such publishing agreement and applicable law.
- © The Author(s), under exclusive licence to Springer Nature Limited 2024

Methods

CMIP5 and CMIP6 models

We analysed 16 climate models with extended simulations to 2299 or 2300 from CMIP5 and CMIP6 depending on data availability: historical runs for the period 1850–2005 (1850–2014) and RCP8.5 (SSP585) scenario runs for the period 2006–2300 (2015–2300) from eight CMIP5 and eight CMIP6 models. For the extension of RCP8.5/SSP585, anthropogenic radiative forcing continues to increase beyond the year 2100, reaching a level slightly above 12 W m^{-2} by 2250, after which it stabilizes and maintains a consistent value^{14,28}. This facilitates the multi-model analyses of ENSO changes under long-term anthropogenic warming. We subtracted a ten-year running mean to remove decadal and longer variability in each variable to investigate ENSO variability. We choose 50 years in the twentieth (1941–1990) and twenty-third (2241–2290) centuries to represent present-day and future climates, respectively. The ENSO variation is represented by the monthly s.d. of the Niño 3.4 index during these two periods. To reveal the time variation of ENSO amplitude, we computed the running 50-year s.d. of the Niño 3.4 index for each model. We also analysed 14 (9) climate model outputs under SSP126/RCP2.6 (SSP245/RCP4.5) depending on data availability to assess the long-term ENSO response under different emission scenarios. Under the RCP2.6/SSP126 extension scenario, radiative forcing reaches 2.6 W m^{-2} in 2100 and then slowly declines, stabilizing at around 2.0 W m^{-2} beyond 2200. For RCP4.5, radiative forcing is held constant at 2100 levels of around 4.5 W m^{-2} beyond 2100^{14,28}. For each model, only one member-run (r1i1p1 or r1i1p2) is analysed in this study. We also analysed the outputs from ACCESS-ESM1-5 large ensembles with extended simulations to 2300 and compared them with the above climate outputs. Each of the ten members is integrated forward under the historical (1850–2014) and future emission scenarios (SSP585 and SSP126 for 2015–2300) with different initial conditions.

Ocean–atmosphere feedbacks

ENSO variations in the eastern equatorial Pacific are controlled by a series of positive and negative ocean–atmosphere feedbacks. On the basis of a heat budget analysis, the growth rate of ENSO SST anomalies can be cast as²⁹

$$R_g = \mu_a \beta_h \left\langle \frac{-H(\bar{W})\bar{W}}{H_m} a_h \right\rangle + \mu_a \beta_w \left\langle \frac{-\partial \bar{T}}{\partial z} \right\rangle + \mu_a \beta_u \left\langle \frac{-\partial \bar{T}}{\partial x} \right\rangle - TD - \left(\frac{\langle \bar{u} \rangle}{L_x} + \frac{\langle -2y\bar{v} \rangle}{L_y^2} + \frac{\langle \bar{W} \rangle}{H_m} \right) \quad (1)$$

Here we are mainly focused on the changes in each ocean–atmosphere feedback term under long-term global warming. The terms on the right side of equation (1) represent thermocline feedback, Ekman feedback, zonal advective feedback, TD and dynamic damping, respectively. T and H_m represent mixed-layer temperature and depth, where H_m is 50 m in this study. u and v indicate the mixed-layer zonal and meridional velocities, respectively. W is the vertical velocity around the base of the mixed layer (60 m). The symbol $\langle \cdot \rangle$ denotes the volume average in the eastern Pacific region ($90^\circ \text{ W} - 170^\circ \text{ W}$, $5^\circ \text{ S} - 5^\circ \text{ N}$), and the overbar represents the monthly climatological mean value. μ_a is the equatorial ($130^\circ \text{ E} - 90^\circ \text{ W}$, $5^\circ \text{ S} - 5^\circ \text{ N}$) wind response to eastern Pacific SSTA forcing. β_u , β_w and β_h represent the responses of central equatorial ($160^\circ \text{ E} - 150^\circ \text{ W}$, $5^\circ \text{ S} - 5^\circ \text{ N}$) zonal currents, eastern Pacific upwelling and zonal SLA slope to anomalous equatorial wind forcing, respectively. a_h describes the subsurface (80 m) temperature response to SLA (Kelvin waves) in the eastern Pacific Ocean. All these responses are estimated from linear regression between different variables. The function $H(x)$, also known as the Heaviside step function, is used to account for only the vertical advection upstream. L_x and L_y are the zonal and meridional extent of the eastern equatorial box, and y is the distance from the Equator.

Prior to the diagnostic analysis, we first calculated the Niño 3 SST skewness to assess the model's capability to simulate realistic ENSO nonlinearity and feedbacks^{8,30,31}. It should be noted that we used

monthly rather than seasonal-mean November–January anomalies at the peak of ENSO for the skewness calculation, resulting in relatively small skewness values in our study. Four of the 16 models simulate negative Niño 3 skewness, contrasting with observations. For instance, ACCESS-ESM1-5 and its large ensemble experiments display strong negative Niño 3 skewness, suggesting the limited capabilities of this model in simulating ENSO nonlinearity and feedbacks. The remaining models successfully simulate positive Niño 3 skewness, aligning with observations. Six models provide direct outputs of vertical velocity (Supplementary Table 1). For the other models, we indirectly calculated the vertical velocity using upward ocean mass transport. However, due to the absence of both vertical velocity and vertical mass transport output, the GISS-E2-H model was excluded from the diagnostic analysis. We therefore diagnosed ENSO feedbacks from ten (four) models (Supplementary Table 1) with positive (negative) skewness in this study.

Impacts of the thermal expansion coefficient

The thermal expansion coefficient is defined as³²

$$\alpha = -\frac{1}{\rho} \left. \frac{\partial \rho}{\partial \theta} \right|_{S,p} \quad (2)$$

where ρ is the density, θ is the potential temperature, S is the salinity and p is the pressure. Here we calculated the thermal expansion coefficient (α) using the Gibbs Sea Water Oceanographic Toolbox on the basis of the International Thermodynamic Equation of Seawater–2010 (ref. 32).

The subsurface temperature anomaly response to a given SLA (or steric height) anomaly could be influenced by the thermal expansion coefficient changes. To evaluate the impacts of the thermal expansion coefficient changes, we initially computed steric height anomalies using ocean temperature and salinity data during 1850–1860. Subsequently, we maintained the salinity and interannual ocean temperature anomalies at their 1850–1860 values, introducing only the background ocean temperature with a ten-year sliding average from 1850 to 2300. We then calculated the steric height and the resultant regression coefficient between subsurface temperature (upper 500 m) and steric height over a ten-year moving window (Extended Data Fig. 6d). This approach ensures that any changes in the regression coefficient are the results of the background ocean temperature and thus thermal expansion coefficient changes.

TOE of reduced ENSO SST variability

We employed a signal-to-noise ratio method to quantify the TOE of ENSO SST variability changes³³. First, we calculated the monthly SST anomalies by subtracting the climatological monthly value for each model. We then filtered out low-frequency signals longer than ten years and calculated the ENSO amplitude change over a 50-year moving window, with a one-year shift forward starting from 1850 to 2300. This results in an evolution of 50-year running variability from 1900 to 2300, with the ending year of each 50-year time window being recorded. The unforced internal variability in ENSO SST variation, defined as the s.d. of the 50-year ENSO amplitude change based on the last 500 years of the piControl run, is considered the background noise. We then calculated future changes in ENSO SST variability by subtracting the present-day (1941–1990) ENSO variation, which we refer to as the signal. We defined the TOE of reduced ENSO SST variability as the year when the signal-to-noise ratio of the Niño 3.4 index falls below a threshold (-1.0) and remains below the threshold (signal-to-noise ratio < -1) thereafter. The TOE is recorded as the last year of the sliding window of emergence. It should be noted that the TOE of the HadGEM2-ES and MRI-ESM2-0 models exceeds 2300 and thus cannot be evaluated with the available data. For simplicity and to minimize its impact on the results, we assigned a TOE value of 2300 to these two models when calculating the median value of TOE. Importantly, this assignment does not impact the final median and interquartile range of the TOE presented in this study.

Bootstrap test

We tested the significance of our results with the bootstrap test³⁴. To examine whether the multi-model mean decrease in ENSO variation is statistically significant, we averaged 16 randomly resampled models from all 16 climate models used in this study, allowing for the possibility of selecting the same model multiple times. This process was repeated 10,000 times to calculate mean and s.d. values for both the twentieth and twenty-first centuries. If the difference in mean values between the two periods is greater than the sum of the s.d. values, the change is considered statistically significant at the 95% confidence level²².

Data availability

All data supporting the findings of this study are openly available. The CMIP6 data can be found at <https://esgf-data.dkrz.de/search/cmip6-dkrz/>. The CMIP5 data can be found at <https://esgf-node.llnl.gov/search/cmip5/>.

Code availability

The code is publicly available via Zenodo at <https://doi.org/10.5281/zenodo.11416550> (ref. 35).

References

- O'Neill, B. C. et al. The Scenario Model Intercomparison Project (ScenarioMIP) for CMIP6. *Geosci. Model Dev.* **9**, 3461–3482 (2016).
- Kim, S. T. & Jin, F.-F. An ENSO stability analysis. Part I: results from a hybrid coupled model. *Clim. Dyn.* **36**, 1593–1607 (2010).
- Cai, W. J. et al. Increased variability of eastern Pacific El Niño under greenhouse warming. *Nature* **564**, 201–206 (2018).
- Kohyama, T., Hartmann, D. L. & Battisti, D. S. Weakening of nonlinear ENSO under global warming. *Geophys. Res. Lett.* **45**, 8557–8567 (2018).
- The International Thermodynamic Equation of Seawater, 2010: Calculation and Use of Thermodynamic Properties* (Intergovernmental Oceanographic Commission, 2010).
- Geng, T. et al. Emergence of changing Central-Pacific and Eastern-Pacific El Niño–Southern Oscillation in a warming climate. *Nat. Commun.* **13**, 6616 (2022).
- Cai, W. et al. Changing El Niño–Southern Oscillation in a warming climate. *Nat. Rev. Earth Environ.* **2**, 628–644 (2021).
- Peng, Q. Collapsed upwelling weakens ENSO under sustained warming beyond the 21st century. *Zenodo* <https://doi.org/10.5281/zenodo.11416550> (2024).

Acknowledgements

Q.P. and S.-P.X. are supported by the National Science Foundation (AGS 1637450). The National Center for Atmospheric Research (NCAR) is sponsored by the National Science Foundation under Cooperative Agreement No. 1852977. We acknowledge high-performance computing support from Cheyenne (<https://doi.org/10.5065/D6RX99HX>) provided by NCAR's Computational and Information Systems Laboratory, sponsored by the National Science Foundation. We thank M. T. Luongo for his help with grammar corrections and suggestions.

Author contributions

Q.P. and S.-P.X. designed the study. Q.P., S.-P.X. and C.D. carried out the analysis. Q.P. wrote the first draft. S.-P.X. and C.D. contributed to writing and editing the manuscript.

Competing interests

The authors declare no competing interests.

Additional information

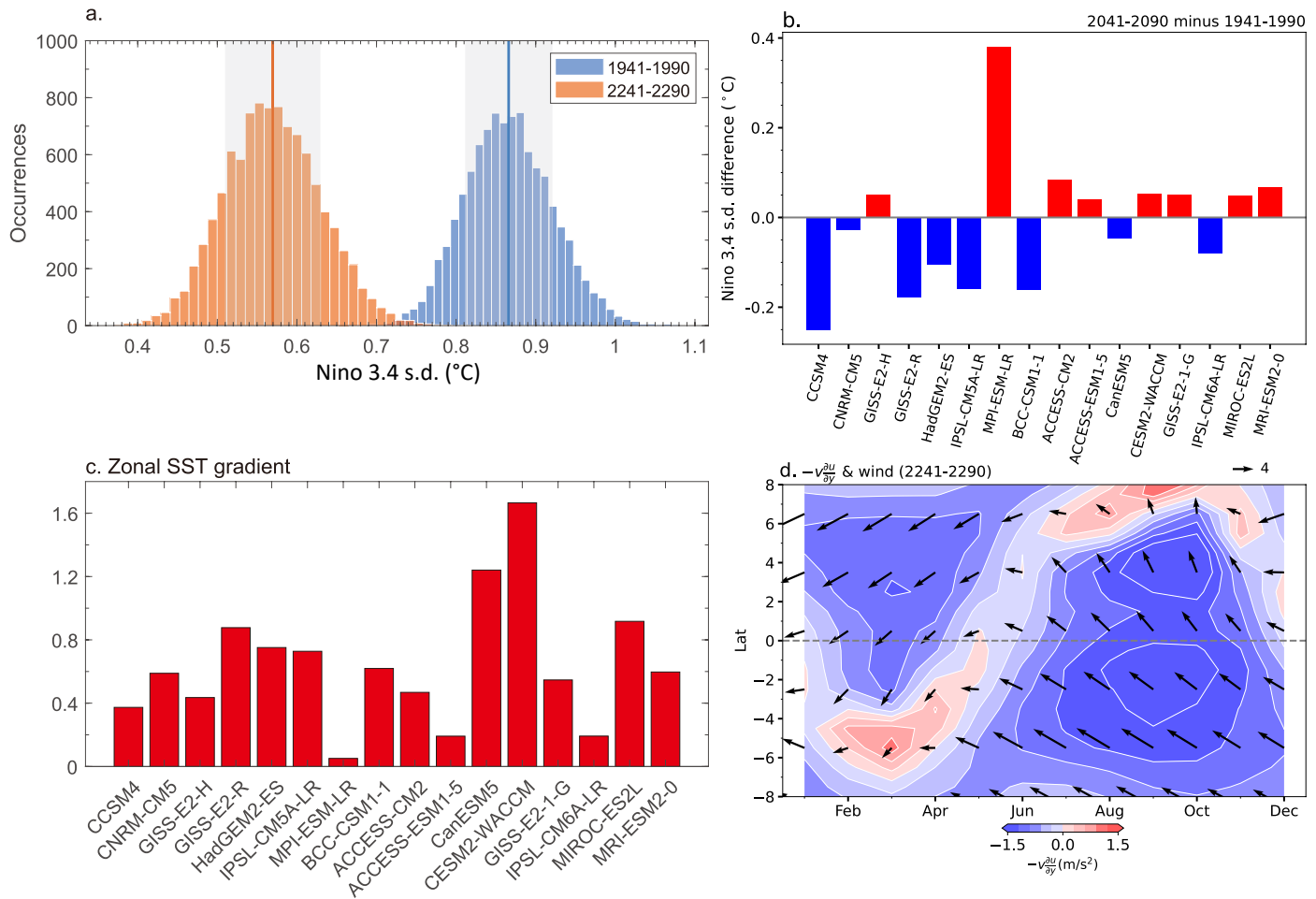
Extended data is available for this paper at <https://doi.org/10.1038/s41558-024-02061-8>.

Supplementary information The online version contains supplementary material available at <https://doi.org/10.1038/s41558-024-02061-8>.

Correspondence and requests for materials should be addressed to Shang-Ping Xie.

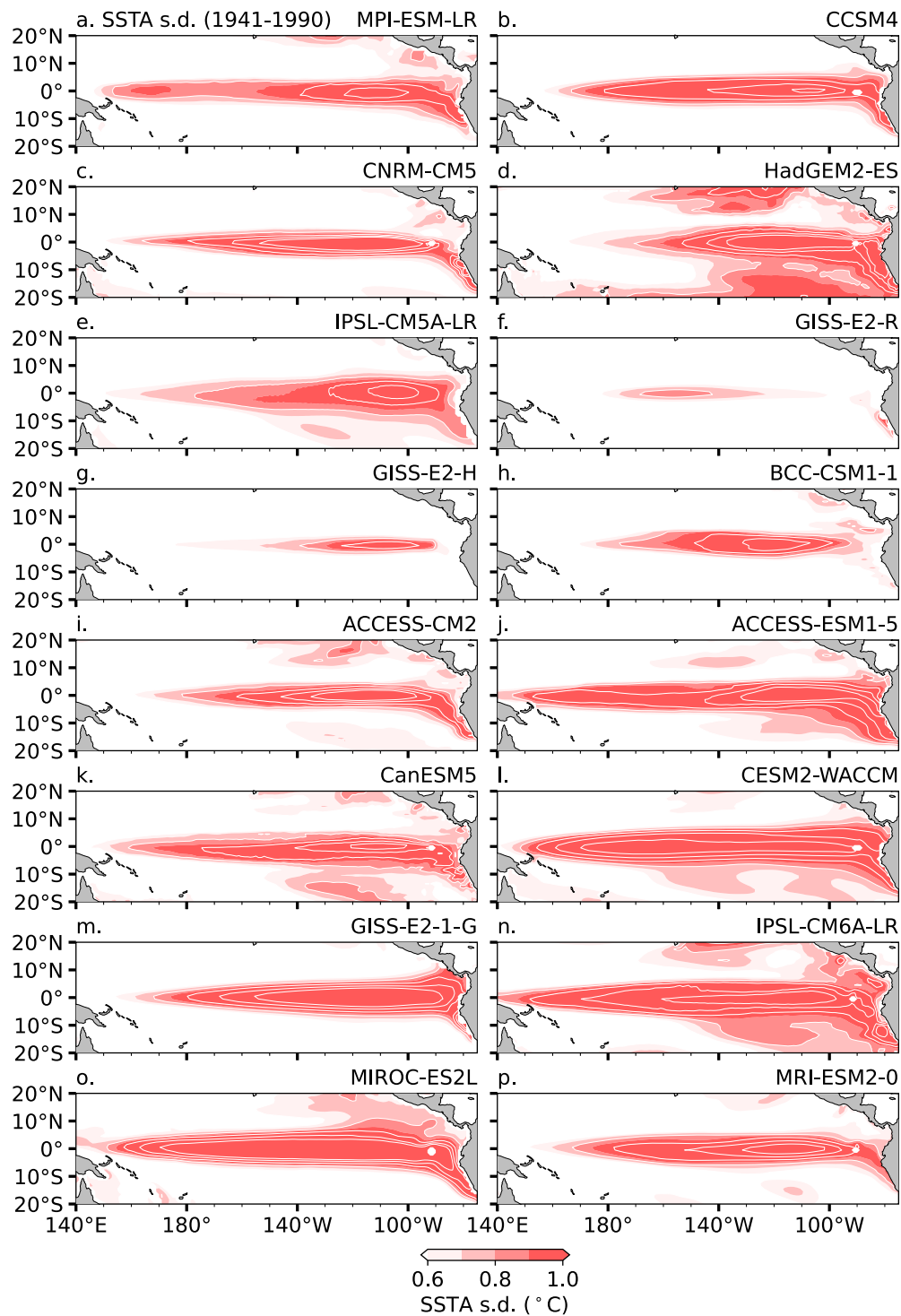
Peer review information *Nature Climate Change* thanks the anonymous reviewers for their contribution to the peer review of this work.

Reprints and permissions information is available at www.nature.com/reprints.

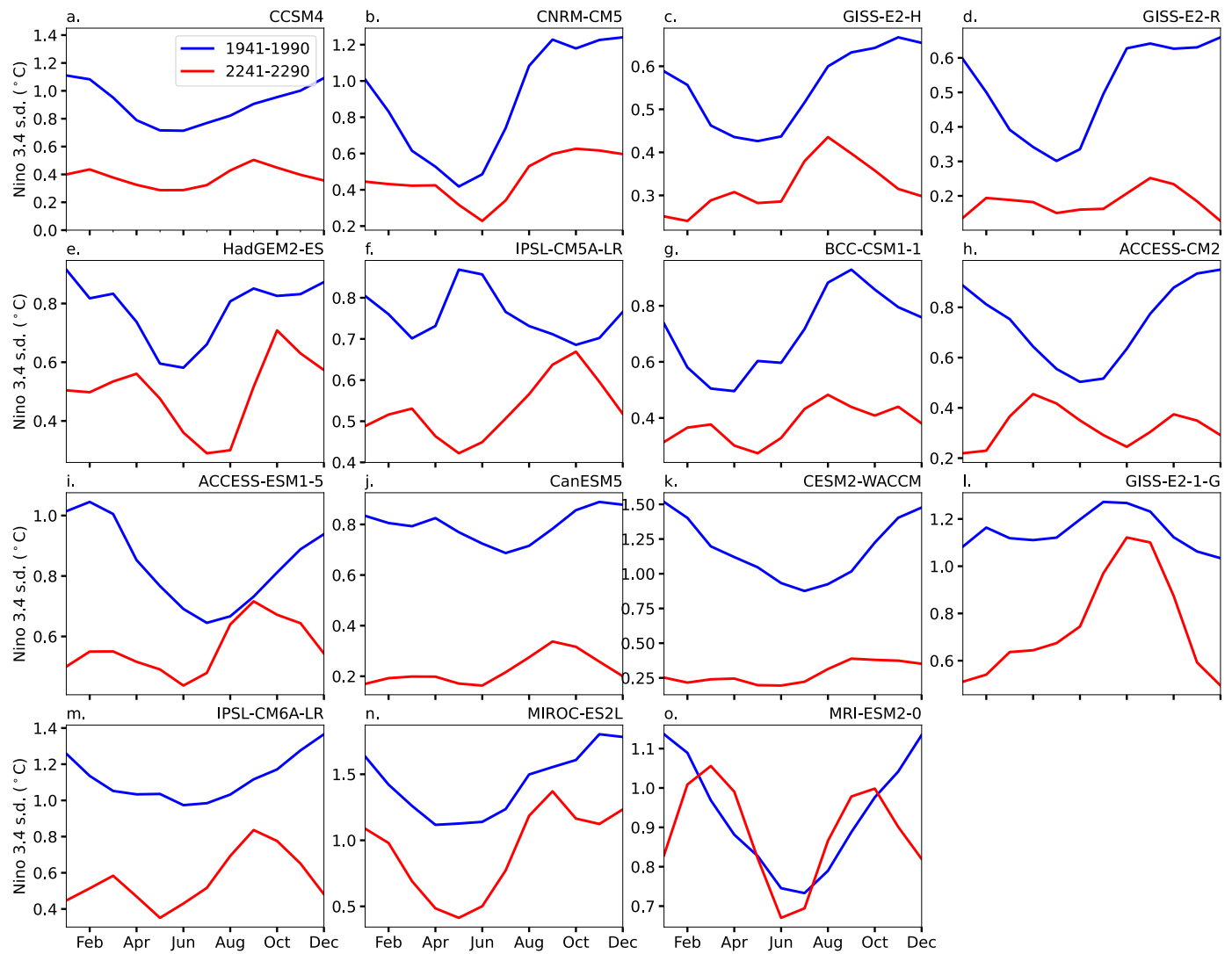


Extended Data Fig. 1 | The projected ENSO variability and mean state changes. (a) Histograms of 10,000 realizations of the Bootstrap method for Niño 3.4 SST standard deviation (s.d.) (°C) in the 20th century (1941-1990, blue) and 23rd century (2241-2290, red). The blue and red lines indicate the mean values of the 10,000 realizations for each period. The grey shaded areas correspond to the respective one s.d. of the 10,000 realizations (see Method). (b) The difference in s.d. (°C) of Niño 3.4 SST anomalies between the 21st-century SSP585/RCP8.5 scenario period (2041-2090) and the historical reference period (1941-1990).

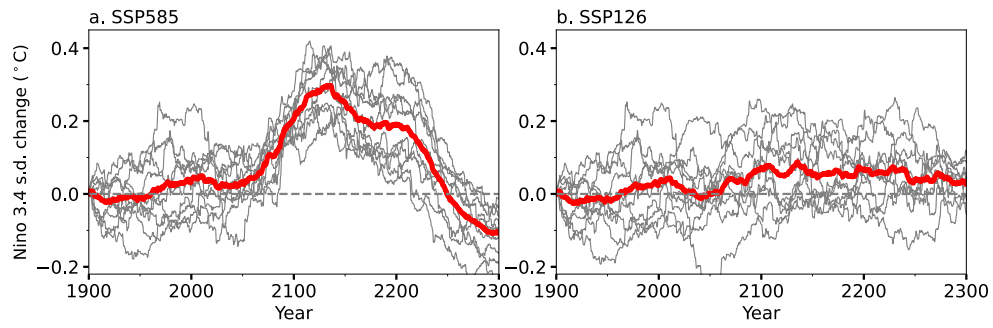
(c) The difference in equatorial Pacific zonal SST gradient between the 23rd (2241-2290) and 20th (1941-1990) centuries under the SSP585/RCP8.5 scenario. Here, zonal SST gradient change is defined as the SST change difference between the eastern (120°W-170°W, 5°S-5°N) and western (150°E-170°W, 5°S-5°N) boxes, with positive values indicating an El Niño-like warming pattern. (d) Latitude-time Hovmöller diagrams of the eastern Pacific (90°W-170°W) zonal mean monthly climatological wind (vectors; m/s) and the $-v^2/2gy$ term (color shading; m/s²) during 2241-2290.



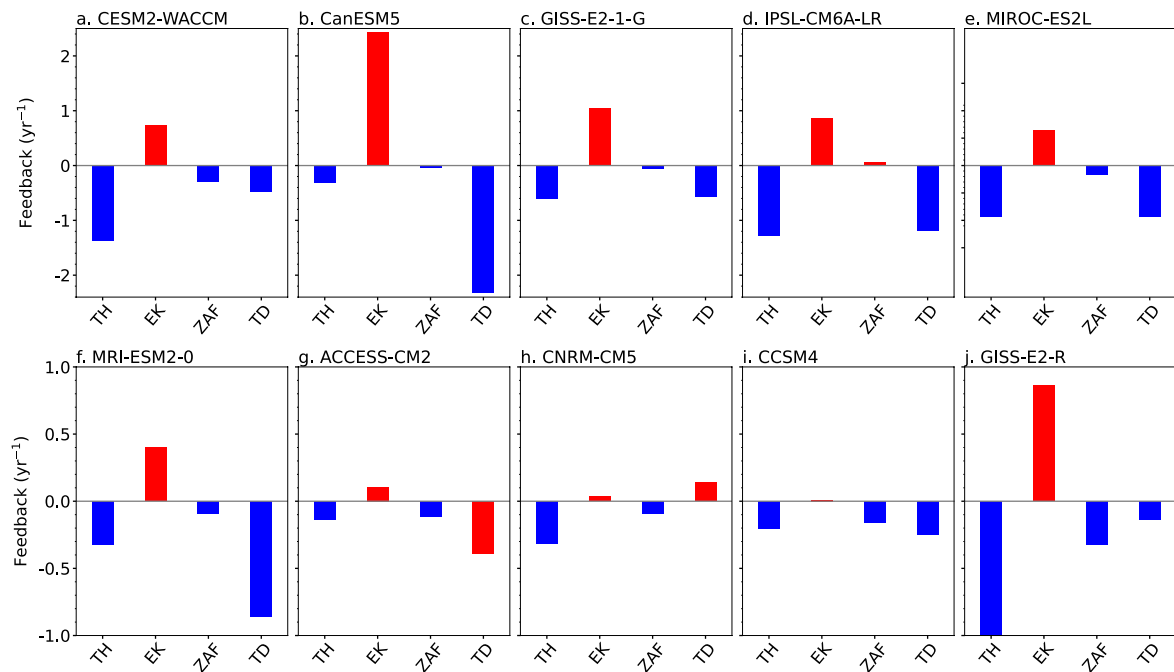
Extended Data Fig. 2 | The ENSO simulations in the 16 climate models. a–p, The simulated spatial pattern of present-day (1941-1990) SSTA s.d. (°C, color shading) from the 15 climate models used in this study.



Extended Data Fig. 3 | The simulated seasonal cycle of ENSO amplitude. a–o, The simulated seasonal cycle of the Niño 3.4 SSTA s.d. from the 15 models with reduced ENSO variability during the historical period (1941-1990) (blue line) and the 23rd-century (2241-2290) (red line) under the SSP585/RCP8.5 scenario.

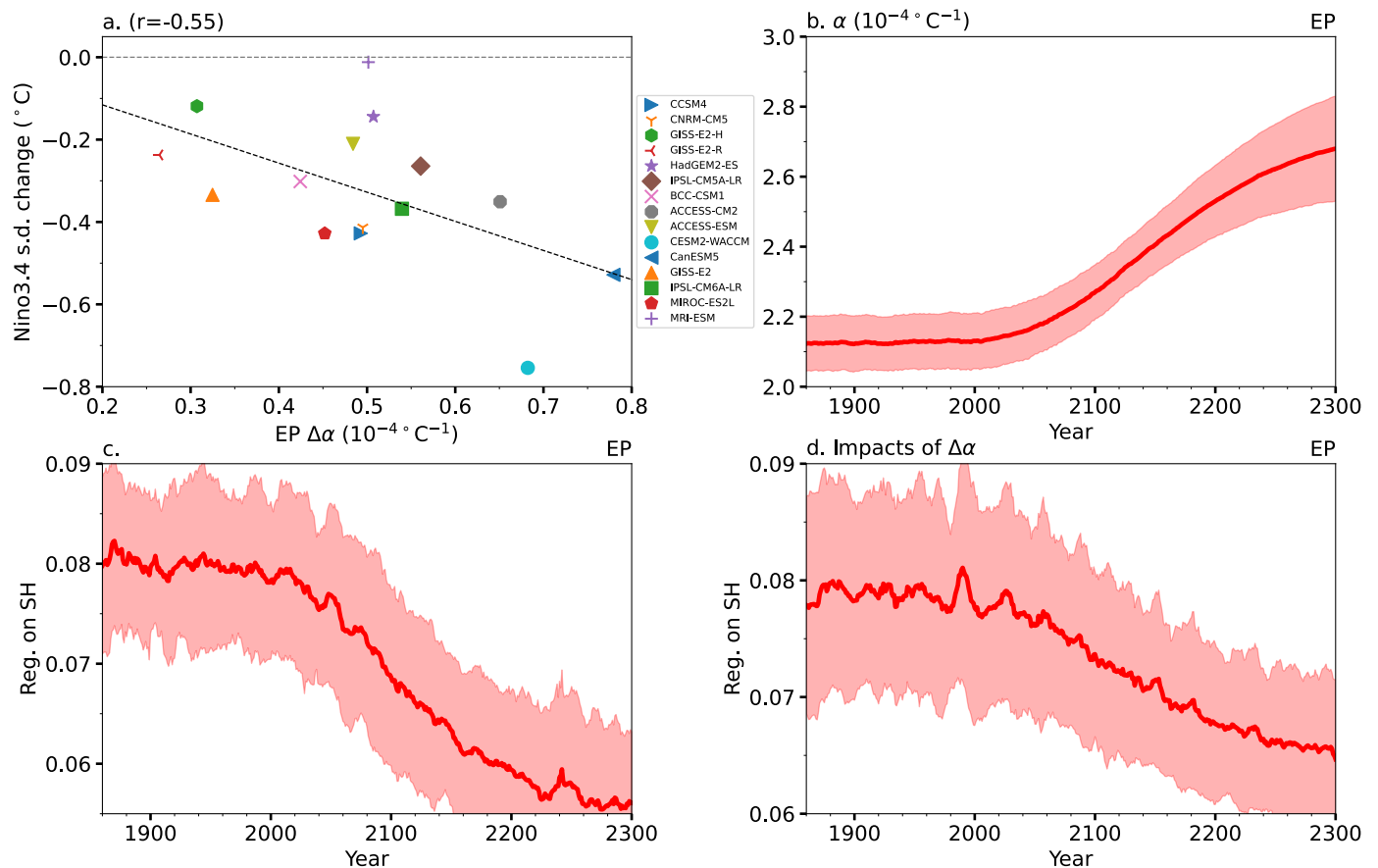


Extended Data Fig. 4 | Time variation of simulated ENSO amplitude from ACCESS-ESM1-5 large ensembles. The running 50-year ENSO amplitude change ($^{\circ}\text{C}$) from ACCESS-ESM1-5 large ensembles during the historical period and under the (a) SSP585 and (b) SSP126 emission scenarios. The ACCESS-ESM1-5 ensemble mean is shown as the thick red curve.



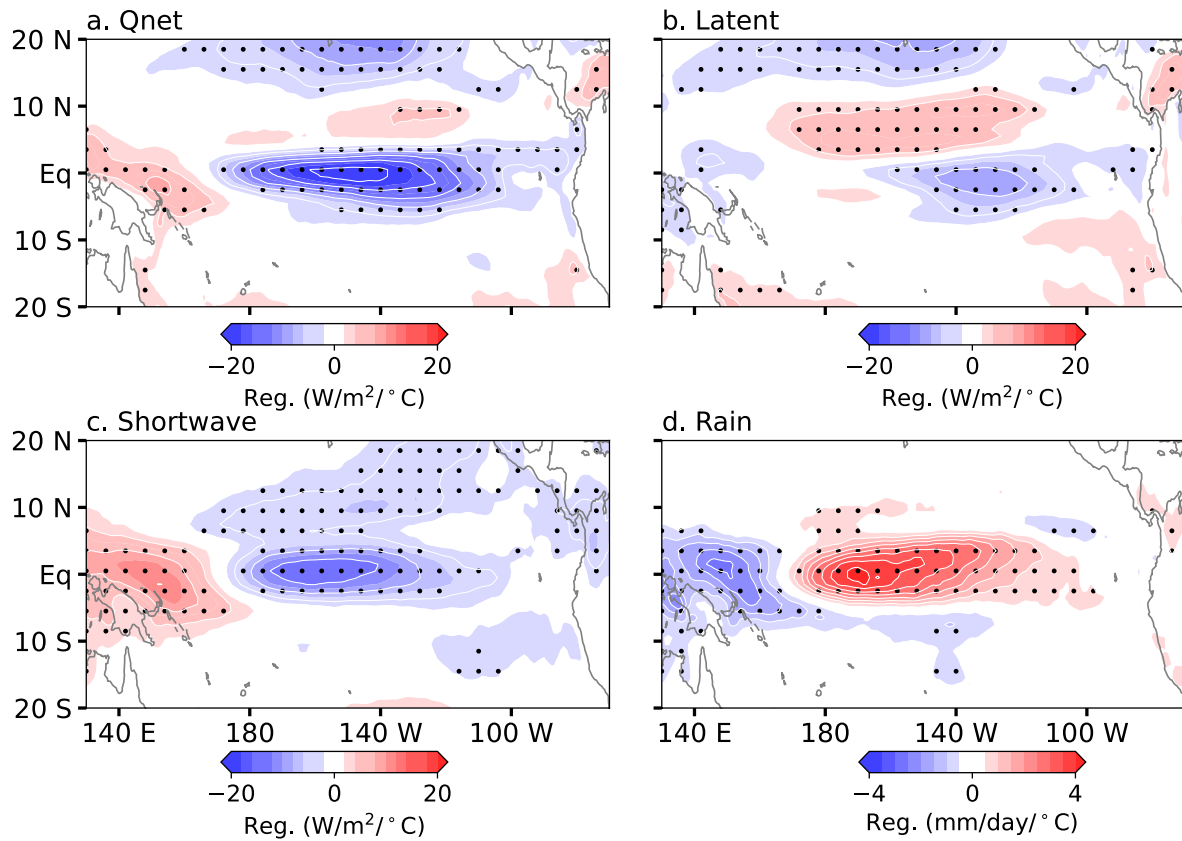
Extended Data Fig. 5 | ENSO-related air-sea feedback changes for each model. a–j, The strength of ENSO-related air-sea feedback changes (yr⁻¹) (see Methods) in the eastern Pacific (5°S–5°N, 90°W–170°W) from each of the ten models with a positive Niño 3 skewness. TH, EK, ZAF, and TD represent thermocline feedback,

Ekman feedback, zonal advective feedback, and thermodynamic damping, respectively. The CNRM-CM5, CCSM4, and GISS-E2-R belong to CMIP5, while the rest are from CMIP6.



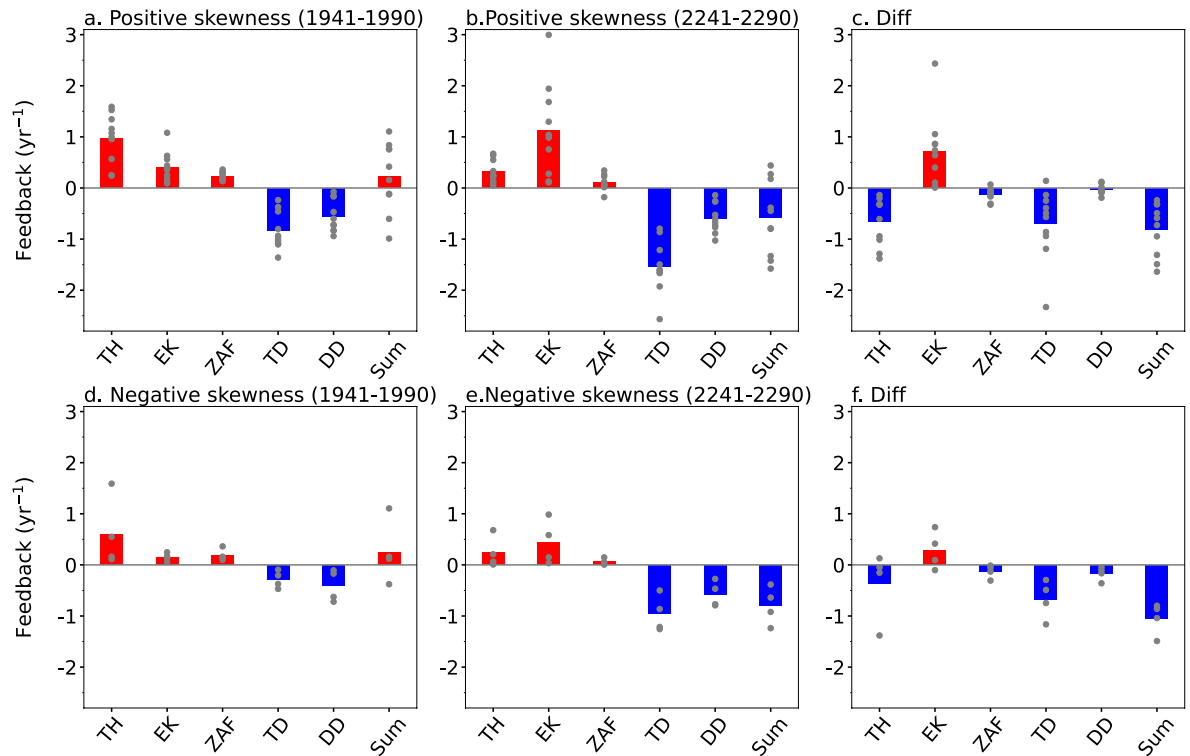
Extended Data Fig. 6 | Impacts of thermal expansion coefficient changes. (a) Scatter plots of eastern Pacific (5°S – 5°N , 90°W – 170°W) averaged thermal expansion coefficient changes ($\Delta\alpha$, $10^{-4}\text{ }^{\circ}\text{C}^{-1}$) and Niño 3.4 SST s.d. changes from SSP585/RCP8.5 extended simulations. The running 10-year upper 500 m averaged (b) α ($10^{-4}\text{ }^{\circ}\text{C}^{-1}$) from the historical and SSP585/RCP8.5 outputs. (c) Regression of upper 500 m ocean temperature ($^{\circ}\text{C}$) against steric height (SH, mm) anomalies averaged in the eastern Pacific Ocean from CMIP6 models.

(d) The impacts of $\Delta\alpha$ on the regression of upper 500 m ocean temperature against SH anomalies (see Methods). The MME is shown as the thick red curve and the color shadings indicate one inter-member standard deviation ($n = 10$) above and below the MME. The regression coefficient is calculated over a 10-year moving window, with a one-year shift forward starting from 1850 to 2300. The results in (b)–(d) are derived from the ten models exhibiting positive Niño 3 skewness (see Methods).



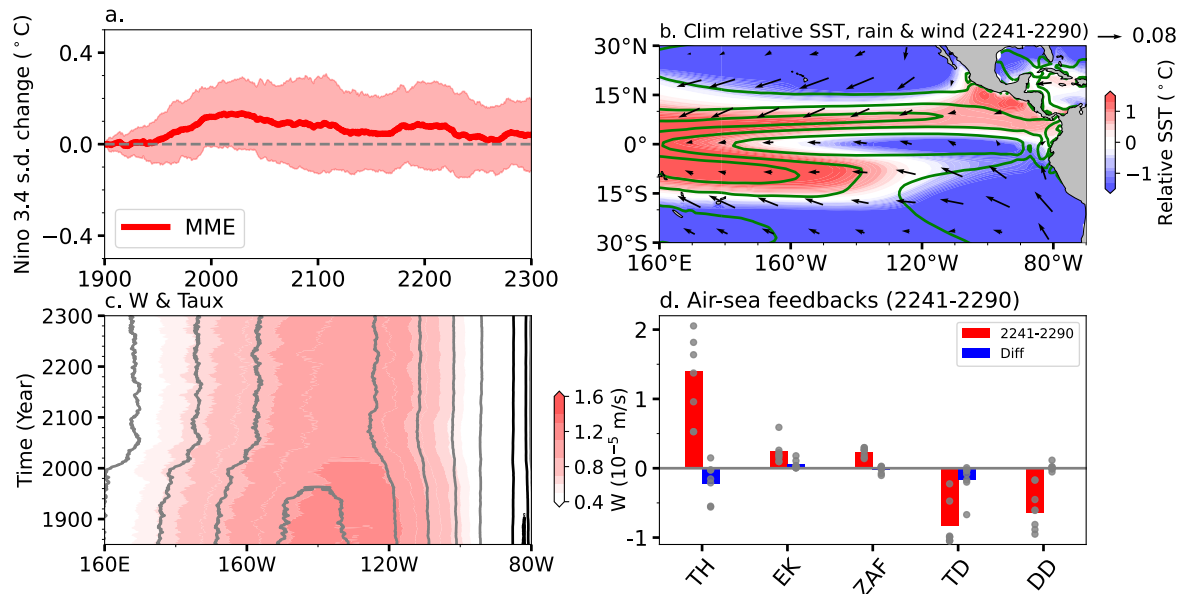
Extended Data Fig. 7 | Thermodynamic response changes to Niño 3.4 SST variability. Projected changes in (a) Qnet (W/m²), (b) latent heat flux (W/m²), (c) shortwave radiation (W/m²), and (d) rainfall (mm/day) response to Niño 3.4 SST anomalies under SSP585 during 2241-2290 relative to the present-day

(1941-1990). These responses are estimated using linear regression between variables and Niño 3.4 SST anomalies from the ten climate models with positive Niño 3 skewness. The stippled areas denote signals that are significant at the 95% confidence level from the bootstrap test.



Extended Data Fig. 8 | ENSO-related air-sea feedback changes among models with positive and negative Niño 3 skewness. a–f, The MME (bars) ENSO-related air-sea feedback (yr^{-1}) in the eastern Pacific (5°S – 5°N , 90°W – 170°W) during the present-day (1941–1990) (left panels), future (2241–2290) (middle panels), and

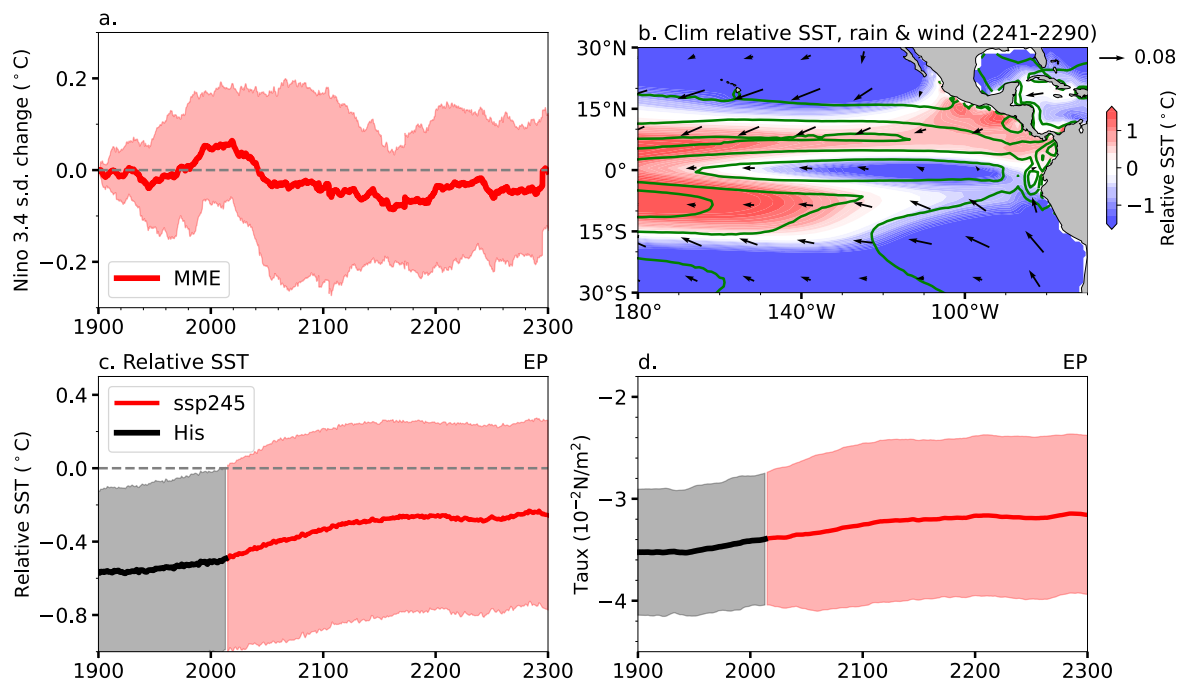
their difference (right panels) across models with positive (upper panels; $n = 10$) and negative (lower panels; $n = 4$) Niño 3 skewness (see methods). The dots indicate individual model results.



Extended Data Fig. 9 | ENSO variation changes under SSP126/RCP2.6.

(a) The MME (thick red curve) running 50-year ENSO variation change ($^{\circ}\text{C}$) from the historical and SSP126/RCP2.6 outputs; the color shadings indicate one inter-member standard deviation above and below the MME ($n = 14$; Supplementary Table 1). (b) Future (2241-2290) mean state relative SST ($^{\circ}\text{C}$, color shading), rainfall (contours with an interval of 3 mm/day; positive in green), and wind stress (N/m^2 , vectors) under SSP126/RCP2.6. (c) The Hovmöller diagram of the

equatorial mean upwelling at 60 m (w ; 10^{-5} m/s , color shading; derived from models with direct vertical velocity outputs), and the zonal wind stress (contours with an interval of $0.01 \text{ N}/\text{m}^2$; positive in black and negative in gray). (d) The MME ENSO-related air-sea feedbacks (yr^{-3}) during 2241-2290 under SSP126/RCP2.6 (red bars) from seven climate models (Supplementary Table 1), along with the differences between these air-sea feedbacks and their present-day counterparts (blue bars); The dots indicate individual model results.



Extended Data Fig. 10 | ENSO amplitude changes under SSP245/RCP4.5.

(a) The running 50-year ENSO variation change ($^{\circ}\text{C}$) from the historical and SSP245/RCP4.5 outputs. (b) Future (2241–2290) annual mean relative SST ($^{\circ}\text{C}$, color shading), rainfall (contours with an interval of 3 mm/day; positive in green), and wind stress (N/m^2 , vectors) under SSP245/RCP4.5. The running 50-year EP

(c) relative SST ($^{\circ}\text{C}$) and (d) zonal wind stress ($10^{-2}\text{N}/\text{m}^2$) from the historical and SSP245/RCP4.5 outputs. The MME is shown as the thick curve, and the color shadings indicate one inter-member standard deviation above and below the MME ($n = 7$; Supplementary Table 1).